Experimental and numerical study of a compact inline swirler for gas–liquid separation

Published Version:
Experimental and numerical study of a compact inline swirler for gas–liquid separation / Maluta F.; Paglianti A.; Montante G.. - In: CHEMICAL ENGINEERING SCIENCE. - ISSN 0009-2509. - ELETTRONICO. - 265:(2023), pp. 118219.1-118219.16. [10.1016/j.ces.2022.118219]

This version is available at: https://hdl.handle.net/11585/900464 since: 2022-11-07

Published:

DOI: http://doi.org/10.1016/j.ces.2022.118219

Experimental and Numerical study of a compact inline swirler for gas-liquid separation

Francesco Maluta*, Alessandro Paglianti, Giuseppina Montante

Dipartimento di Chimica Industriale 'Toso Montanari', Alma Mater Studiorum – Università di Bologna, Viale del Risorgimento 4, 40136 Bologna, Italy

*francesco.maluta@unibo.it

Abstract

The liquid mean and fluctuating velocity field, the pressure drop, the gas-phase distribution and the bubble size distribution in a compact inline swirler for gas-liquid separation were experimentally measured. The results served as validation for the proposed computational approach and the most suitable turbulence model was identified. The gas phase distributions obtained considering both a constant bubble diameter and the local bubble size distribution (BSD) through the solution of a Population Balance Equation (PBE) confirmed the lighter gas phase accumulation towards the pipe centre. The study highlights that to realistically predict the BSD a coupled solution of the PBE with the flow equations is needed and that the resulting distribution is relatively narrow. The gas accumulation zone obtained coupling the solution of the PBE is in good agreement with the experimental one. It is shown that CFD may help the design of inline swirlers for gas-liquid separation.

Keywords: CFD, Population Balance Equation, Turbulence model, PIV, Pressure Drop, Bubble Size Distribution

1. Introduction

The separation of multiphase mixtures exploiting swirling flows is a well-known operation in chemical and process engineering, with applications in solid-liquid, liquid-liquid, gas-solid and gas-liquid processes [1]. The working principle relies on the generation of a rotating motion that produces angular accelerations larger than the gravitational acceleration that can enhance and speed-up the separation due to the density difference of the phases constituting the mixture [2]. Exploiting a force larger than the gravitational one, results in smaller equipment and lower investment cost to production ratio [3], thus enforcing one of the principle of process intensification proposed by Stankiewicz and Moulijn [4]. The rotating flow can be generated either by moving parts, as for instance in the centrifuges typically adopted in pharmaceutical industries, or by static geometrical details, such as the case cyclones adopted for gas-solid separation [5]. Larger separation efficiencies are obtained when the rotating flow is generated by moving parts, leading to higher operating costs.

For all the aforementioned reasons, gas-liquid separators, such as static swirling flow devices placed inside pipes, have been receiving increasing attention in the recent years, especially in applications related to energy production. For instance, these devices are being successfully applied to coalbed methane wells to reduce the liquid content [6] and in the fission gas removal systems in Thorium Molten Salt Reactors (TMSR) [7]. On the other hand, the industrial application of static inline swirling flow devices for gas-liquid separations is hindered by the relative high pressure drop, compared to vessel-type separators. Moreover, their sensitivity to flow rates makes them not suitable for widely varying flow rates [8]. The study of these static separators can help in analyzing and troubleshooting their limiting aspects and widening their adoption in several industrial applications.

One promising tool to study inline static swirling separators is Computational Fluid Dynamics (CFD). CFD can provide information on the gas-liquid fluid dynamics in real-size systems without the need to scale-down the equipment to fit in a laboratory, thus eliminating the need to transfer the results from the pilot to a full-scale plant. Furthermore, several operating conditions and separator design solutions can be tested [9], limiting the need for prototypes. However, since the literature on the topic is still in its developing stage, any computational approach must be validated with experimental campaigns to ensure that the numerical simulations are reliable and robust [10]. CFD has been adopted since the very first numerical studies on static swirling separators [11], in which a very dilute gas-liquid mixture was separated with a static inline swirler in nuclear applications. Different design solutions were tested with a Reynolds Averaged Navier-Stokes (RANS) approach. An early attempt to apply the baseline model for bubbly flows developed for the Euler-Euler Two Fluid Model (TFM) [12] to the gas-liquid flow in inline static helical swirlers was proposed by Zidouni et al. [10]. The authors highlighted the limitations in the modelling approach due to the neglected bubble-bubble interaction and due to the monodispersed bubble size approximation. The modelling approach by Zidouni et al. was then validated and tested on a vertical swirl generating device by Putra et al. [9]. In this study the local comparison of numerically determined gas volume fraction with results obtained with high-resolution gamma-ray computed tomography was performed. The authors did not overcome the mono-dispersed approximation, but they tested several constant bubble diameters and a bimodal distribution, concluding that the results were strongly influenced by the bubble size. The same computational approach was also adopted in the comparative numerical simulations of different inline swirlers [13] adopting a bi-modal bubble size distribution and renouncing the solution of a population balance model (PBM). To the best of authors knowledge, the only study on static inline swirlers that couples a PBM to the RANS equations is the work by Yuan et al. [14] in which the authors solve a population balance equation (PBE) with the Taylor expansion method of moments (TEMOM). The authors consider a one way coupling between the liquid flow and the gas phase and solve the model equations just inside the static inline swirler, without tracing the flow evolution downstream of the separator.

In this work both experimental and numerical investigations are conducted to characterize a compact inline swirler for gas-liquid separation. The single-phase liquid flow field is experimentally determined with the Particle Image Velocimetry (PIV) and the pressure drop is measured with a differential pressure manometer. Digital Image Analysis (DIA) is adopted to determine the bubble size in the proximity of the central core region of gas accumulation and to track the evolution of this zone along the pipe length. From a computational point of view, the TFM-RANS equations are solved both with a constant bubble diameter and coupled with a PBE, comparing the predicted gas distribution with the experimental results. Different turbulence models are evaluated, and a computational approach for such systems is proposed as a tool to identify the size of the central core of gas accumulation.

The manuscript is organized as follows: firstly, the system and the experimental techniques are introduced, then the flow equations, the PBM and the numerical solution procedure are presented. The results of the grid independence study are then reported, followed by the single and two-phase comparison of different turbulence models with the experimental results. The results of the PBE solved both in a frozen flow field and coupled with the flow equations are then presented, focusing on bubble size distribution and on the size of the central core region of gas accumulation. Lastly conclusions are drawn.

2. Investigated System and experimental techniques

An inline compact swirling device (also called swirler, for short) was positioned inside a plexiglass straight horizontal pipe of diameter D equal to 0.09 m. The pipe was 3.5 m long before the swirler and 3.5 m after, to allow for the complete development of the flow inside the pipe. The swirler consisted of a central cylindric hub of 25mm from which 6 flat blades, tilted at 45° from the pipe and hub axis, extended up to the pipe internal walls. The blades had a 2mm thickness and the total axial length of the swirler was 13 mm, making the design of the swirler extremely compact with respect to other inline separators [13]. The system, which is schematically depicted in Figure 1, was operated at room temperature both with just a liquid phase, consisting of tap water (density, ρ_L = 998 kg/m^3, viscosity μ_L = 0.001 Pa s) and a mixture of air (density, ρ_G = 1.225 kg/m^3, viscosity μ_G = 1.79×10^{-5} Pa s) and water.

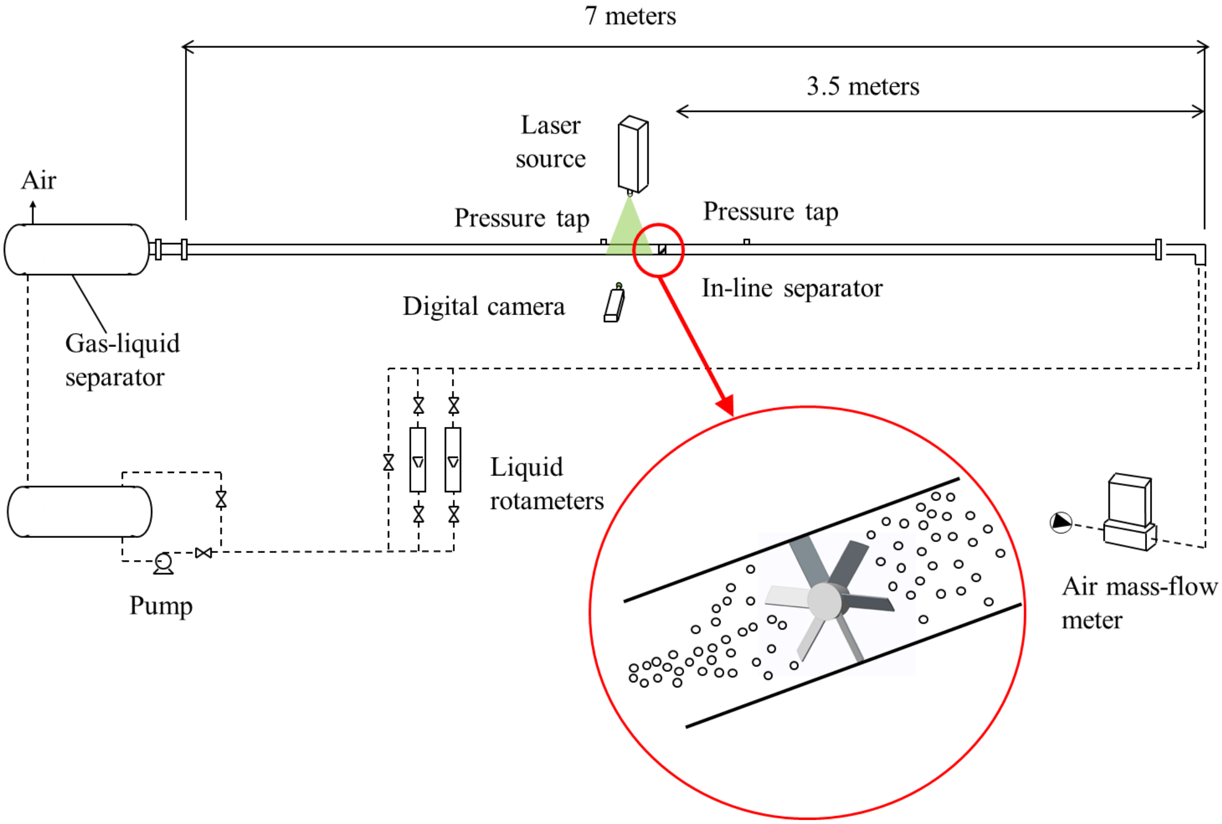

Figure 1 – Sketch of the experimental rig

For the experiments in single-phase conditions, a water volumetric flow rate equal to 20m^3/h, corresponding to a mean liquid velocity equal to 0.87m/s, was considered. For the gas-liquid analysis a liquid volumetric flow rate of 25m^3/h and a gas volumetric flow rate of 7.5L/h were considered, corresponding to a mean mixture velocity equal to 1.11m/s, with a gas volume fraction of 1.77%.

The single-phase velocity field was measured by means of Particle Image Velocimetry (PIV). Data were collected on a portion of a vertical diametrical plane, located downstream the swirler. A pulsed Nd:YAG laser (λ = 532nm, 65mJ) sheet lighted the investigating area. As previously done in measuring the flow field in stirred tanks [15], talc powder was adopted for seeding the liquid, for cheaply obtaining a good laser light scatter towards a Charge-Coupled Device camera (resolution of 1344 × 1024 pixels) handled by a Dantec Dynamics synchronization and acquisition system. Based on the Sauter mean diameter of 13 μm and the density of 2820 kg/m^3, the talc particles were found to be a suitable tracer, having a relaxation time very close to the value of classical liquid seeding particles and a Stokes number well below unity. The instantaneous velocity vectors were obtained on a square grid of 1.28mm side from the adaptive PIV correlation of 5000 camera images collected in double-frame mode. The time interval between the two laser pulses was set to 300 μs. Preliminary tests ensured statistical convergence of mean velocities and turbulent fluctuations, as shown by the velocity profiles in Figure 2. A validation procedure discarded the instantaneous vectors that not fulfilled two criteria one based on the evaluation of the peak heights in the correlation plane and the other on the velocity magnitude. Based on a cartesian coordinate system with the origin located on the centre of the downstream surface of the swirler and the z-axis aligned with the axis of the pipe, the PIV data were collected in a vertical diametrical section of total length of 75 mm, starting at the z coordinate equal to 60 mm (green section in Figure 3). From the instantaneous flow field, the mean axial (corresponding to the z-velocity component) and the vertical velocity components, U and V, and the axial and vertical root mean square (rms) velocity fluctuations, u and v, were obtained. The y coordinate is positive if directed to the top of the pipe, the z coordinate is positive if directed towards the tube outlet.

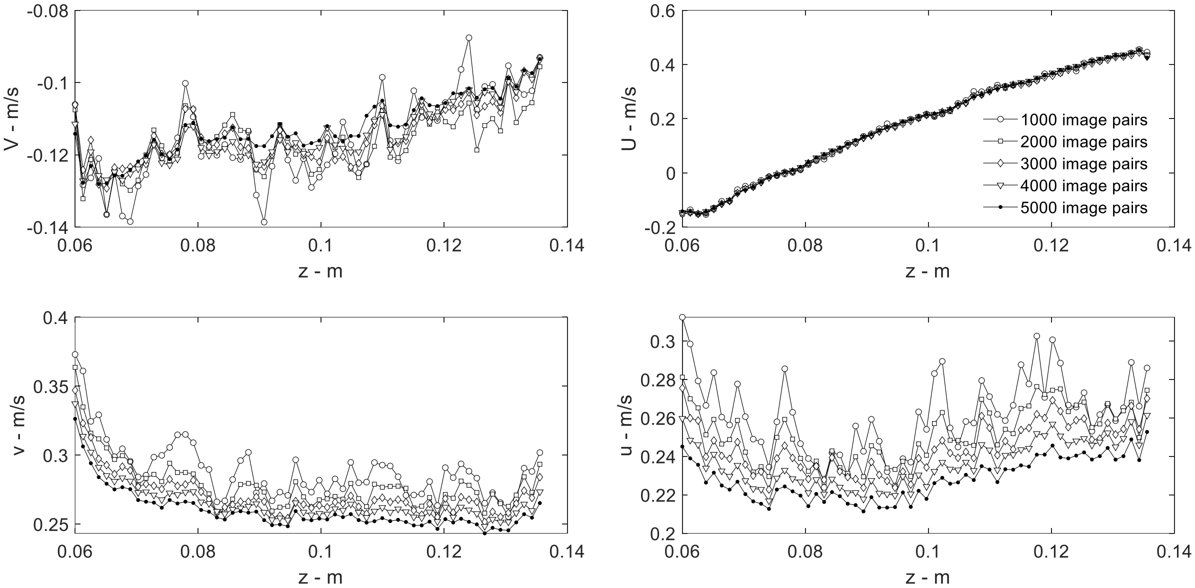

Figure 2 – Experimental axial profiles of mean vertical and axial velocity, V and U, and vertical and axial root mean square (rms) velocity fluctuations, v and u. Velocities are collected at y=0 and a liquid flow rate of $20m^3/h$, without gas. The measurements were obtained with a different number of image pairs

A differential manometer was employed to measure the concentrated pressure drop due to the inline separator. Two sampling zones located 1 m before and 2.16 m after the swirler were considered. The pressure drop due to the swirler was obtained as the pressure drop measured with the swirler minus the (distributed) pressure drop due to the pipe, measured without the swirler.

In gas-liquid conditions, the camera view for the bubble size distribution (BSD) measurements was located at 0.45m < z < 0.56m (yellow section in Figure 3). The BSD was obtained by capturing and processing 400 images, collected in single frame mode. The pipe was illuminated adopting a diffused/incoherent light emitted by five tubular neon lamps at 50 kHz. The number, dimensions and position of the lamps were chosen for obtaining an almost uniform illumination of the selected pipe portion. The camera was placed at the pipe side opposite with respect to the lamps, thus enhancing the contrast between the image background and the bubble shadow. The exposure time was optimised to avoid the distortion effects due to the bubble motion. Only the bubbles contained in the thin slab identified by a focal depth of a few millimetres were measured; in this way a reliable calibration factor could be adopted. The calibration factor between the CCD pixels and the real images was determined by means of an object of known size placed in the focused region. The images were analyzed with the Canny algorithm, based on the identification of local maxima of the image gradients—the gradient being calculated using the derivative of a Gaussian filter [16]. The analysed zone was outside the central core of gas accumulation, and it extended radially up to the pipe wall, since in this zone the bubbles are not clustered, and they can be easily identified. Overall, about 20,000 bubbles were identified to obtain the bubble size distribution, ensuring statistically significant measurements. With the adopted technique and configuration, the minimum detectable bubble size was equal to 0.6mm.

In addition, four hundred pictures of a pipe section were collected in the region located at $0.31m < z < 0.46m$ (red section in Figure 3) in the gas-liquid operation. The images were converted in grayscale and from 4 pictures the grey values corresponding to a portion of pipe devoid of bubbles were taken. The average of the 400 frames was calculated and it was normalized between the gray value corresponding to just liquid and the maximum white level corresponding to the zones with high gas hold up, in order to normalize the picture from 0 to 1. The external pipe portion was cropped since the reflection on the pipe walls produced optical disturbances and the resulting image allows to obtain the shape and size of the central zone of gas accumulation.

3. CFD simulations

The set of equations solved in this work are presented in this section. Firstly, the equations for the determination of the single and two-phase flow are presented, together with the formulation of the interphase forces coupling the momentum conservation equations for each phase. The gas-liquid simulations were preliminarily run assuming a constant bubble diameter, then the bubble size was calculated from the solution of a population balance equation, which is presented in Section 3.2).

3.1 Flow Equations

The Reynolds averaged formulation of the Two-fluid model equations assuming steady state, incompressible fluids and isothermal conditions read as:

$$\nabla \cdot (\alpha_i \rho_i \boldsymbol{u_i}) = 0 \tag{1}$$

$$\nabla \cdot (\alpha_i \rho_i \boldsymbol{u_i} \boldsymbol{u_i}) = -\alpha_i \nabla P + \alpha_i \rho_i \boldsymbol{g} + \nabla \cdot (\boldsymbol{\tau_i} + \boldsymbol{\tau_i^t}) + \boldsymbol{F_D} + \boldsymbol{F_{TD}} \tag{2}$$

With α_i, ρ_i and $\boldsymbol{u_i}$ being the volume fraction, the density, and the mean velocity of phase i, respectively, P being the mean pressure shared by the phases, **g** being the gravitational acceleration, $\boldsymbol{\tau_i}$ and $\boldsymbol{\tau_i^t}$ being the laminar and the Reynolds stress tensor, respectively, and the two last terms, $\boldsymbol{F_D}$ and $\boldsymbol{F_{TD}}$, being the interphase drag and turbulent dispersion force. For single phase calculations, $\alpha_i = \alpha_L = 1$ and no interphase forces were considered. Both in single and two-phase calculations, the Reynolds stress tensor was calculated by adopting three different turbulence models: the standard k-ε turbulence model, the k-ω shear stress transport (SST) turbulence model and the Reynolds stress model, RSM, as implemented in Ansys Fluent. The description of these three well-known turbulence models is omitted, and information can be found elsewhere [17,18]. Regarding the extension of these models to multiphase flows, the so-called dispersed formulation is adopted [19], as implemented in ANSYS Fluent 2020R2.

For improving the stability of the simulation when the solution of the PBE was coupled with the flow equations, just the drag and the turbulent dispersion interphase forces were considered. Moreover, for bubbly flows in horizontal pipes a small effect of the lift and the wall lubrication force on the fluid velocities and gas distribution is reported [20]. The interphase drag force can be expressed as:

$$\boldsymbol{F_D} = \frac{3}{4 d_B} \rho_L \alpha_L \alpha_G C_D \lVert \boldsymbol{u_G} - \boldsymbol{u_L} \rVert (\boldsymbol{u_G} - \boldsymbol{u_L}) \tag{3}$$

Where d_B is the bubble size and C_D is the drag coefficient. In Eq. 3 the presence of both the gas and the liquid volume fractions derives from a force balance in an Eulerian frame [21,22] and it was demonstrated to limit the interphase force where gas segregation occurs [23]. The drag coefficient was described with the Ishii and Zuber model [24], as previously done for a similar system [9]. The model assumes different drag coefficients depending on the shape of the bubbles and it reads as:

$$C_D = \max\left(C_D^{sphere}, \min\left(C_D^{ellipse}, C_D^{cap}\right)\right) \tag{4}$$

With C_D^{sphere}, $C_D^{ellipse}$ and C_D^{cap} being the drag coefficients of spherical, ellipsoidal, and spherical cap bubbles. The C_D^{sphere} is obtained from the Schiller and Naumann correlation [25] as a function of the bubble Reynolds number, Re_B:

$$C_D^{sphere} = \frac{24}{Re_B}\left(1 + 0.15 Re_B^{0.687}\right) \tag{5}$$

The $C_D^{ellipse}$ is obtained from Eq. 6 as a function of the Eotvos number, Eo Eq.7, and C_D^{cap} is assumed equal to 8/3:

$$C_D^{ellipse} = \frac{2}{3}\sqrt{Eo} \tag{6}$$

$$Eo = g(\rho_L - \rho_G) d_B^2 / \sigma \tag{7}$$

With σ being the interfacial tension between air and water assumed equal to 0.072 N/m.

The turbulent dispersion force was modelled with the Favre Averaged Drag (FAD) model as proposed by Burns et al. [26], and it reads as:

$$\boldsymbol{F_{TD}} = \frac{3}{4 d_B} \alpha_L \alpha_G C_D \frac{\mu_L^t}{Sc_L^t} \|\boldsymbol{u_G} - \boldsymbol{u_L}\| \left(\frac{\nabla \alpha_G}{\alpha_G} - \frac{\nabla \alpha_L}{\alpha_L}\right) \tag{8}$$

Where μ_L^t is the turbulent viscosity and Sc_L^t is the liquid phase turbulent Schmidt number equal to 0.9.

3.2 Population Balance Equation

In order to close the set of equations presented in Section 3.1) a bubble size must be provided. In this work either a single constant bubble diameter or a population of bubbles with different diameters are considered. In this section the population balance equation, PBE, solved to determine the bubble size in the system is presented.

The bubble size number density function (NDF), $n(d_B)$, transport equation can be expressed as follows:

$$\frac{\partial n(d_B)}{\partial t} + \nabla \cdot (u_G n(d_B)) = B^B + B^C - D^B - D^C \tag{9}$$

Where on the right-hand side of Eq. 9 the birth, B, and the death, D, discrete source terms due to breakup and coalescence events are reported.

The breakup birth and death rates are described by Eq. 10:

$$B^B - D^B = \int_{d_B}^{\infty} \frac{\Omega(d_B, \delta_B)}{n(d_B)} \times n(d_B) d\delta_B - b(d_B) n(d_B) \tag{10}$$

Where the total breakage frequency, $\Omega(d_B, \delta_B)$, and the breakage frequency function, $b(d_B)$, are modelled with the Luo and Svendsen [27] breakup model, which assumes that binary breakage of bubbles is determined by the energy level of the colliding eddies [28]. The total breakage frequency can then be expressed as:

$$\frac{\Omega(d_B, \delta_B)}{n(d_B)} = 0.923(1 - \alpha_G) \left(\frac{\varepsilon}{d_B^2}\right)^{1/3} \int_{Z_{min}}^{1} \frac{(1+Z)^2}{Z^{\frac{11}{3}}} \exp\left(\frac{-12 c_f(d_B, \delta_B)\sigma}{\beta \rho_L \varepsilon^{\frac{2}{3}} d_B^{\frac{5}{3}} Z^{\frac{11}{3}}}\right) dZ \tag{11}$$

With d_B and δ_B being the parent and child diameter, respectively, ε being the turbulent dissipation rate of the liquid phase, Z being the ratio between the size of the eddy and the diameter of the bubble, β being a model constant equal to 2.045 and c_f being the so-called surface energy increase constraint, defined as:

$$c_f(d_B, \delta_B) = \left(\frac{d_B^3}{\delta_B^3}\right)^{\frac{2}{3}} + \left(1 - \frac{d_B^3}{\delta_B^3}\right)^{\frac{2}{3}} - 1 \tag{12}$$

The lower limit of integration in Eq. 11 is assumed as $Z_{min} \sim (11.4 \div 31.4)\eta$, with η being the Kolmogorov length scale. The breakage frequency function can be obtained from the total breakage frequency as:

$$b(d_B) = \frac{1}{2} \int_0^{\frac{d_B}{2^{\frac{1}{3}}}} \frac{\Omega(d_B, \delta_B)}{n(d_B)} \frac{3\delta_B^3}{d_B^3} d\delta_B \tag{13}$$

Where the term multiplying the integral accounts for binary breakage.

The birth and death rates due to coalescence phenomena are obtained as:

$$\begin{aligned} B^C - D^C = \frac{1}{2} \int_0^{d_B} a\left((d_B^3 - \delta_B^3)^{\frac{1}{3}}, \delta_B\right) n\left((d_B^3 - \delta_B^3)^{\frac{1}{3}}\right) n(\delta_B) d\delta_B \\ - n(d_B) \int_0^{\infty} a(d_B, \delta_B) n(\delta_B) d\delta_B \end{aligned} \tag{14}$$

With $a(d_B, \delta_B)$ being the aggregation kernel, consisting of two parts, the collision frequency and the coalescence efficiency [29]. In this work it was assumed that bubble collisions are dominated by turbulence fluctuations. The collision frequency was modelled with the kernel proposed by Prince and Blanch [30], which has a similar expression to the one derived by Coulaloglou and Tavlarides [31] assuming isotropic turbulence. The coalescence efficiency is defined as the ratio of the time required for bubbles to coalesce and the contact time between bubbles, and it was also described with the model proposed by Prince and Blanch [30] assuming bubbles with mobile surface. The resulting aggregation kernel reads as:

$$a(d_B, \delta_B) = \frac{\pi\sqrt{2}}{4} \varepsilon^{\frac{1}{3}} (d_B + \delta_B)^2 \left(d_B^{\frac{2}{3}} + \delta_B^{\frac{2}{3}}\right)^{\frac{1}{2}} \exp\left(-\gamma \frac{\varepsilon^{\frac{1}{3}} \rho_L^{\frac{1}{2}}}{\sigma^{\frac{1}{2}}} \left(\frac{1}{d_B} + \frac{1}{\delta_B}\right)^{-\frac{5}{6}}\right) \tag{15}$$

Where the exponential quantifies the coalescence efficiency and the model constant $\gamma = 1.7$ contains information regarding the initial and final liquid film thickness between the two colliding bubbles. Those two values were taken equal to the original values proposed by Prince and Blanch [30].

Several breakup and coalescence kernels were developed for bubbly flows [29]. More advanced models consider the whole turbulence spectrum [32–34] to obtain breakup and coalescence rates, thus describing particle discrete events not only in the inertial subrange but also in the dissipation range [33]. These advanced models require higher computational costs. For this reason, as a first attempt to couple the TFM with the solution of PBE in pipes with compact swirlers, simpler and computationally cheaper kernels were firstly investigated. Future work may address a detailed comparison between experimental and numerical BSD, obtained with more advanced kernels.

The population balance equation presented was solved with the Quadrature Method of Moments (QMOM) [35]. The moment transform was applied to Eq.9, thus obtaining the transport equation for the moments of the NDF [29]. In order to mathematically close the set of equations, the generic moment of order k, M_k, was then estimated with a quadrature approximation resulting in:

$$M_k = \int_0^\infty n(d_B){d_B}^k dd_B \approx \sum_{i=0}^{N_Q} w_i \xi_i^k \tag{16}$$

Where N_Q is the approximation order, w_i are the quadrature weights and ξ_i are the quadrature abscissas or nodes. In this study, N_Q was taken equal to three and the three weights and nodes are obtained from the solution of the transport equations of the first 6 moments of the NDF through the well-known Product-Difference algorithm [35]. The QMOM solution method is particularly convenient since it is quite computationally cheap and it allows for a fast calculation of the Sauter mean diameter, as the ratio of the third and second moment of the NDF, which is adopted in Eq.3 and Eq.8 for the calculation of the interphase forces.

3.3 Numerical Solution Procedure

The numerical simulations were run in ANSYS Fluent 2020 R2. A computational domain matching the geometry described in Section 2 was designed, with a pipe section 0.9m long before the swirler, equal to 10 pipe diameters, and a 0.91m long pipe section downstream the swirler, as shown in Figure 3. The sections before and after the swirler allowed for a fully developed flow inside the pipe. The geometry was then discretized with three different meshes.

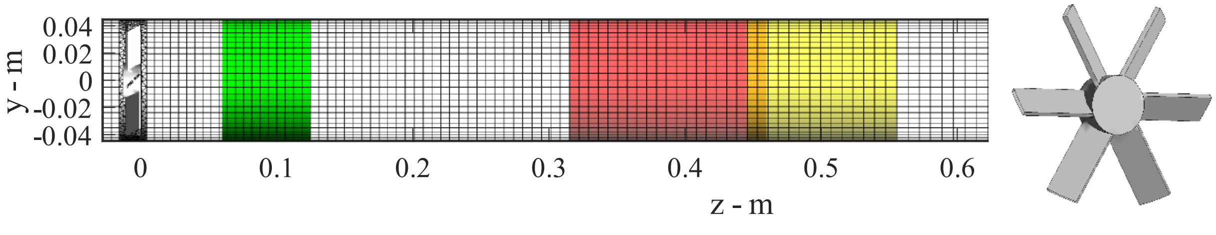

(a) (b)

Figure 3 – Cutaway drawing of the system geometry discretized with the coarsest mesh (a) and the swirler (b). The portion of pipe upstream the swirler and the terminal portion of the pipe are not shown. In green it is highlighted the vertical pipe section in which the single-phase PIV measurements are performed, in red the vertical section in which the gas-liquid measurement of the central core is performed and in yellow the vertical section in which the bubble size distribution was measured. The orange zone derives from the partial overlapping of the red and yellow zones.

The swirler volume was discretized with tetrahedral cells while the rest of the pipe was discretized with hexahedral cells and the cells nodes between these different regions matched univocally, thus producing a conformal interface. The coarsest mesh consisted of nearly 200’000 cells and the finer meshes were obtained by subsequently dividing the edges of each cell in two, thus obtaining an intermediate mesh of around 1’500’000 cells and a fine mesh of 11’600’000 cells.

At the solid walls of the system no-slip boundary conditions for both phases were enforced. The fluid inlet was modelled as a velocity inlet, and the system outlet was modelled as a pressure outlet with a 0-gauge pressure.

The second order upwind discretization scheme was adopted for the momentum equations and the transport of turbulent variables, while the QUICK scheme was adopted for the volume fraction. The moment transport equations were discretized with the first order upwind scheme for stability purposes.

The model equations in single-phase simulations were solved with a steady state solver. The converged flow field was used as initial conditions for the two-phase simulations with a constant bubble diameter.

A pseudo-transient approach with pseudo-time-steps of 0.001 s was adopted, to enhance the solution stability. The coupled solution of the flow equations and the PBE was achieved with a transient second order implicit solver with a time step of 0.001s, starting from the converged gas-liquid flow field obtained with a constant bubble diameter. 40 internal iterations for time step were employed and a total time of 4.2 seconds were simulated, following preliminary sensitivity tests.

Convergence was evaluated by monitoring the scaled residuals which reached a plateau with values of the order of 10^{-5}. The simulations were stopped once the velocities measured in several positions along the pipe reached a constant value, the average volume fraction inside the system did not change anymore and the total mass of fluid exiting the pipe equalled the total mass of fluid entering the system. When the solution of the PBE was performed, also the Sauter mean diameter in several positions was monitored until it reached the steady state.

4. Grid independence study

Single phase simulations with a water volumetric flow rate of Q_L = 20m^3/h were run with the three turbulence models introduced in Section 3.1. The pressure drop obtained as the difference between the average pressure on a cross sectional pipe section just upstream the swirler and one just downstream is shown in Figure 4 as a function of the grid resolution, together with the volume average turbulent dissipation rate, $< \varepsilon >$.

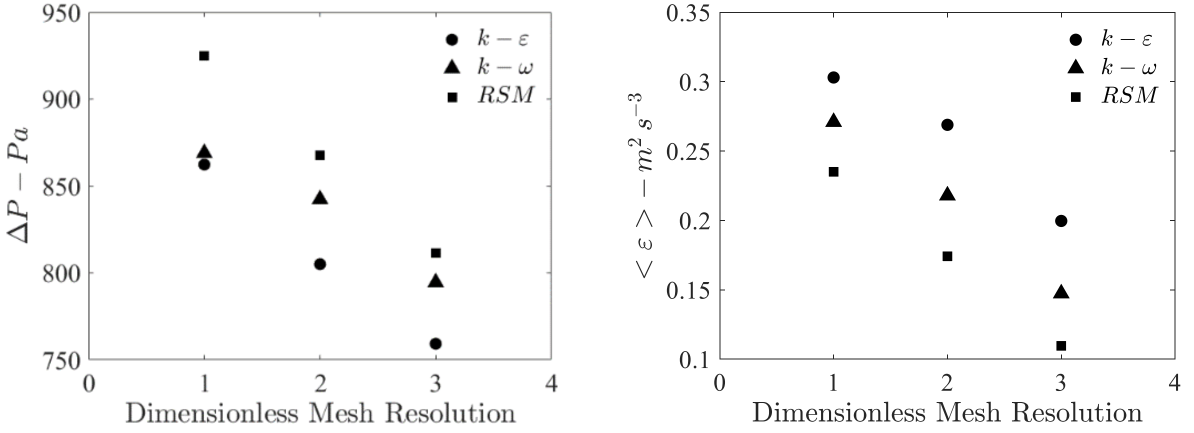

(a) (b)

Figure 4 – Average pressure drop in the swirler zone (a), and volume average turbulent dissipation rate (b) as predicted by different turbulence models and grids with different linear resolution.

The dimensionless mesh resolution in Figure 4 is the average edge size in the swirler zone normalized with the finest mesh average edge size in the same zone, therefore the higher this parameter, the coarser the mesh. For each model, the pressure drop calculated with the coarse grid differs less than 15% from the same value obtained with the fine grid. The intermediate mesh requires less than 13% of the computational cost required by the fine grid and the pressure drop deviations from the fine mesh results is around 6% for each model, confirming that the predictions on the mean flow variables are close to grid independency. The experimentally determined pressure drop is equal to 1005 Pa, and it can be observed that all the models underpredict such value, with deviations around 14% for the k-ε and the k-ω models and around 8% for the RSM. The volume average turbulent dissipation rate obtained with the coarse grid is underpredicted by 34%, 45.6% and 53.4% by the k-ε, the k-ω and the RSM models, respectively, with respect to the predictions with the fine grid. The $< \varepsilon >$ deviations between the intermediate and fine grids are equal to 11.6%, 19.4% and 26.8%, with the k-ε, the k-ω and the RSM models, respectively. These results confirm that in RANS simulations finer grids are required to obtain grid independent turbulent variables, with respect to mean flow variables [36].

Since a further grid refinement would prohibitively increase the computational costs, the Richardson extrapolations [37] on the pressure drop and on the volume average turbulent dissipation rate were calculated to estimate the numerical uncertainties. The extrapolation obtained with the three turbulent models shows that the pressure drop obtainable with an infinitely dense grid differs less than 5% from the experimental value, proving that the computational approach can realistically predict the pressure drop. The volume average turbulent dissipation rate obtained from the experimental pressure drop is equal to 0.38 m^2/s^3. The Richardson extrapolations on $<\varepsilon>$ underpredict the experimental value by less than 6%, with all the models considered. The results of the grid independence study are reported in Table 1.

Table 1 – results of the grid independence study

	# of cells	Linear resolution - m	ΔP - Pa			<ε> - m^2/s^3		
			k-ε	k-ω	RSM	k-ε	k-ω	RSM
Fine	11’580’278	5.2×10^{-4}	862	869	925	0.30	0.27	0.24
Intermediate	1’447’428	0.0010	805	842	868	0.27	0.22	0.17
Coarse	194’907	0.0016	759	795	811	0.20	0.15	0.11
Richardson Extrapolation			1005	960	1003	0.35	0.36	0.37

The pressure drop power, obtained as $\Delta P \cdot Q_L$, was compared with the integral of the turbulent dissipation rate over the whole mass in the system. A discrepancy of about and 33% was observed with the predictions obtained with the RSM with the fine mesh, while a value of 20% was observed with both the k-ε and the k-ω models with the same mesh. These results are in agreement with what was observed by other authors in the numerical simulation of similar systems [38,39]. The underprediction of the turbulent variables may affect the results obtained from the solution of the PBE. On the other hand, the kernel parameter values usually derive from fitting procedures based either on simplified model or on CFD simulations performed in relatively coarse grids. As a consequence, a more accurate description of the turbulent field may not improve the agreement between experimental and numerical BSD [40]. To overcome the uncertainties related to the underprediction of the turbulent dissipation rate in the calculation of the coalescence and breakage rates, grid independent kernel parameters [40] and grid-dependent corrections [40,41] on the turbulent variables were proposed. Nevertheless, no scalar corrections and grid independent parameters were adopted in this preliminary study. From this analysis it emerges that the results are not entirely grid independent, but grid independent results in the present case are unaffordable due to the large computational costs required. Adopting the fine grid leads to moderate improvements in the prediction accuracy of the mean flow and turbulent variables with respect to the intermediate grid. Conversely, the computational costs are almost one order of magnitude different. For these reasons, the finest grid was adopted just for single-phase calculations, whereas the intermediate grid was adopted for gas-liquid simulations.

5. Results

In this section the single-phase results are compared against the experimental measurements, successively the gas-liquid predictions obtained with a constant bubble diameter are analyzed and lastly the results from the coupled solution of the flow equations and the PBE are discussed.

5.1 Single-phase comparison of different turbulent models

In this section the predictions obtained with different turbulent models are compared with experimental data and observations. Single phase simulations performed with the fine mesh and a liquid flow rate of $20m^3/h$ are compared against the PIV measurements in the same operative conditions to assess the accuracy of the results. The accuracy of the different turbulence models is discussed, and the most suitable model is identified and selected for the coupling of the PBE solution.

The single-phase liquid velocity components on a plane reproducing the investigation area of the PIV are shown in Figure 5, Figure 6 and Figure 7. In this work, the axis origin is positioned at the centre of the hub, on the face downstream the swirler, and the z-axis is coincident with the pipe axis. Figure 5 shows that the mean axial liquid velocity is higher towards the walls of the pipe and that a low mean liquid velocity zone is found close to the pipe axis. In fact, the swirler imparts a rotation of the flow and the solid central hub offers a resistance to the flow towards the pipe centre. The slow-velocity central region is qualitatively well predicted by the k-ε model that better predicts the axial acceleration in this zone, compared with the k-ω and the RSM model. In particular, the k-ω model slightly shifts the mean liquid velocity profiles towards higher axial coordinates while preserving the qualitative mean velocity distribution pattern. Conversely the RSM does not predict the mean axial velocity gradients of neither the central slower zone nor the periphery. The velocity distribution may be affected by the slight geometrical differences between the experimental rig and the computational domain, therefore some of the discrepancies may be due to this effect, especially at higher radial coordinates.

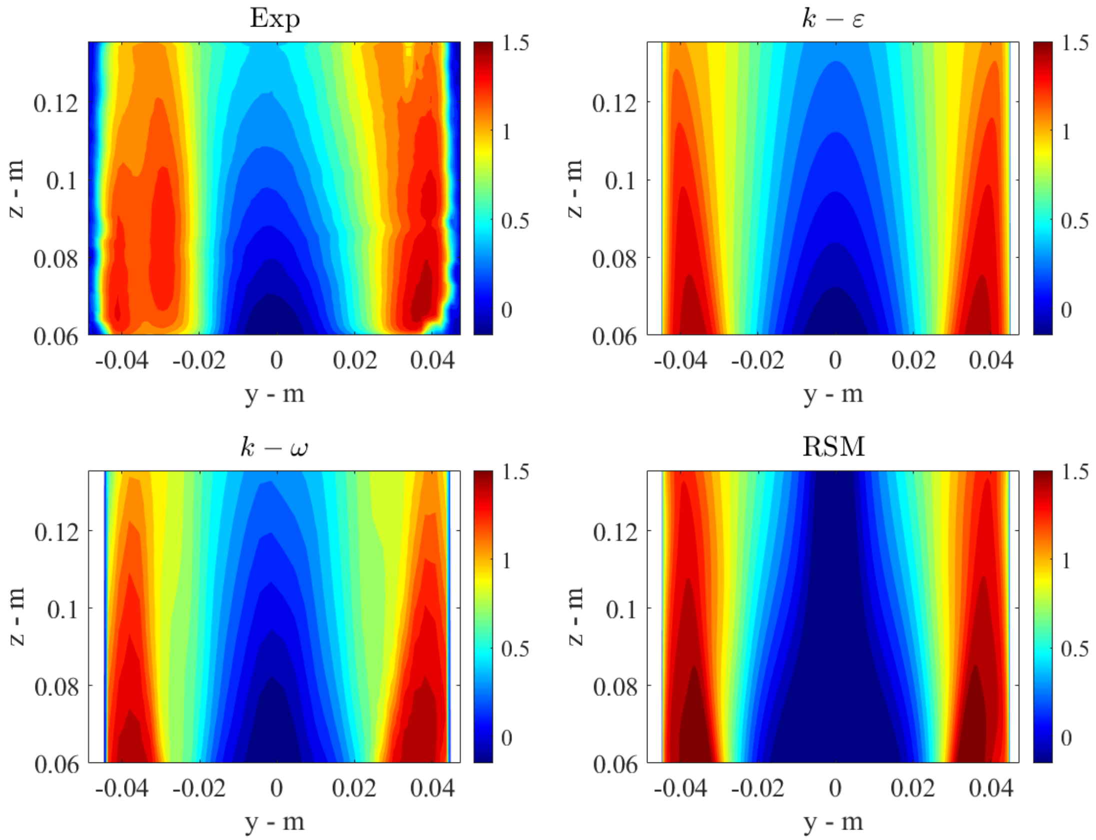

Figure 5 – mean axial liquid velocity distribution on a plane downstream of the swirler as measured from the PIV (Exp) and as obtained from the simulations with different turbulence models. The liquid is flowing from bottom to top, and the color scale is in m/s.

Figure 6 shows that all the turbulent models underpredict the mean y-velocity component magnitude. The asymmetrical distribution of the mean radial liquid velocity is correctly described by the numerical simulations, but the minimum velocity magnitude is underpredicted almost by a factor of two. The mean liquid vertical velocity component magnitude, which is equal to the radial velocity magnitude since the plane is collected at a x=0 coordinate, is around an order of magnitude smaller than the mean axial component. Therefore, even relatively large percentual variations may result in secondary absolute mean liquid velocity differences.

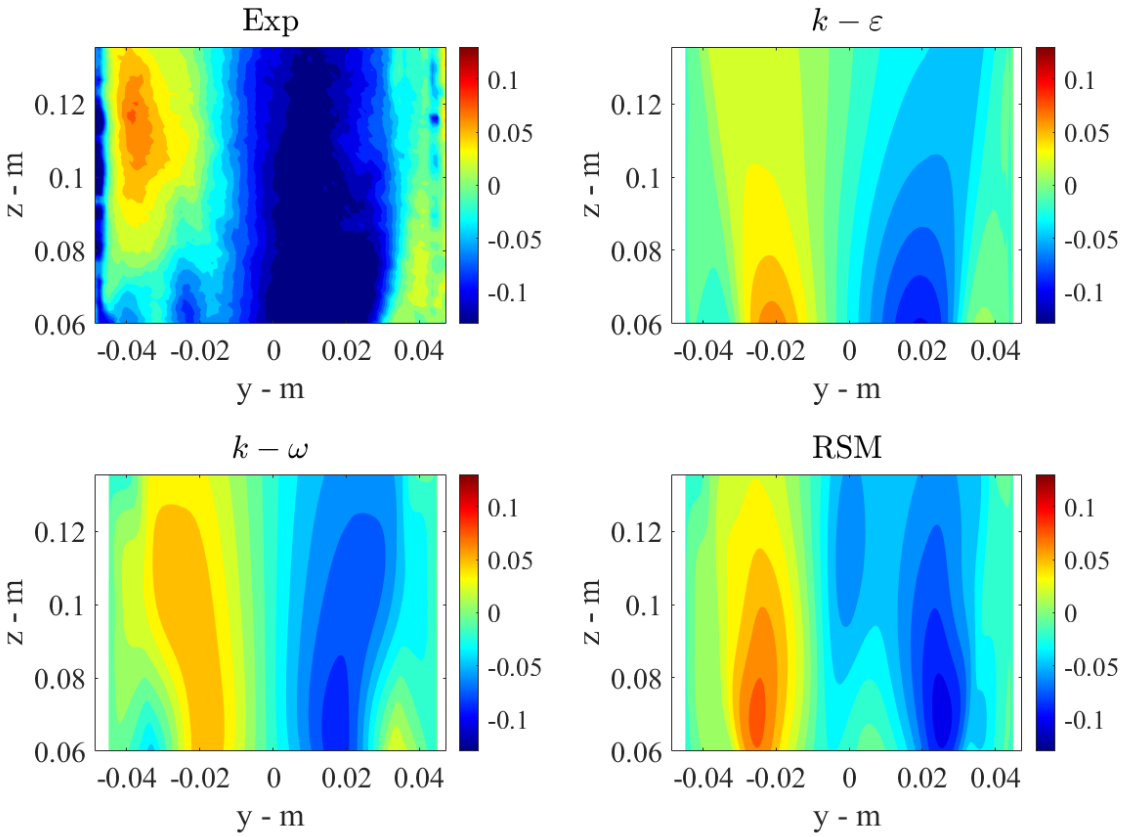

Figure 6 – mean liquid y-velocity distribution on a plane downstream of the swirler as measured from the PIV (Exp) and as obtained from the simulations with different turbulence models. The liquid is flowing from bottom to top, and the color scale is in m/s.

The third out-of-plane x-velocity component of the liquid was not experimentally measured, but from the CFD simulations its magnitude is found to be less than half the mean liquid axial velocity magnitude, as shown in Figure 7.

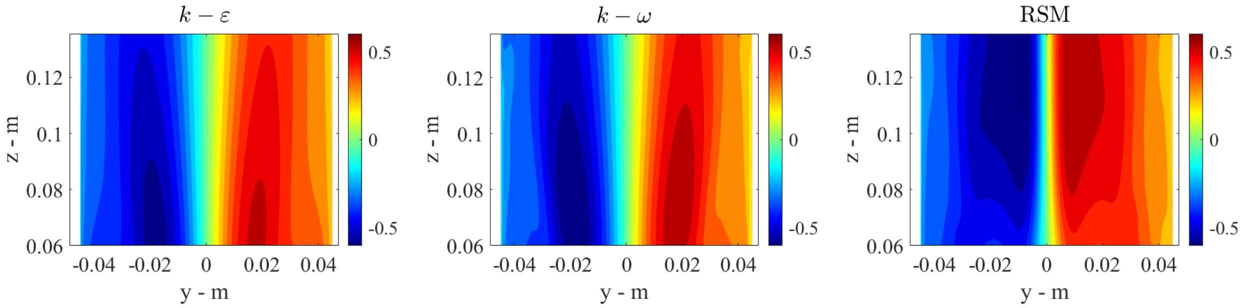

Figure 7 - mean liquid x-velocity distribution on a vertical plane downstream of the swirler as obtained from the simulations with different turbulence models. The liquid is flowing from bottom to top, and the color scale is in m/s.

Figure 7 shows that very similar mean x-velocity fields are predicted by the k-ε and the k-ω models, with a maximum velocity magnitude found at a radial coordinate of about 0.02 m. These two turbulence models predict a maximum in the magnitude of the mean x-velocity position that shifts towards higher radial coordinates as the flow moves from the swirler towards the exit. Conversely, the RSM predicts an opposite trend, with the radial position of the maximum mean x-velocity magnitude migrating towards the centre of the pipe as the flow moves away from the swirler.

To quantitatively assess the agreement between the numerical predictions and the experimental results, several mean liquid velocity profiles at different coordinates were compared. By means of example, the mean axial velocity profiles in Figure 8 confirm the qualitative observation drawn from the maps. Namely, the k-ε model predicts mean axial velocity profiles that better agree with the experimental measurements and the mean y-velocity magnitude is underpredicted by each model. Since the flow is mainly developed in the axial direction, this could explain why the k-ε model qualitatively and quantitatively better agrees with the experimental results. Since the intermediate grid was adopted for the simulation of the gas-liquid flow, as stated in Section 4, in the following figures the velocity profiles obtained with said grid are reported as well, to assess its accuracy.

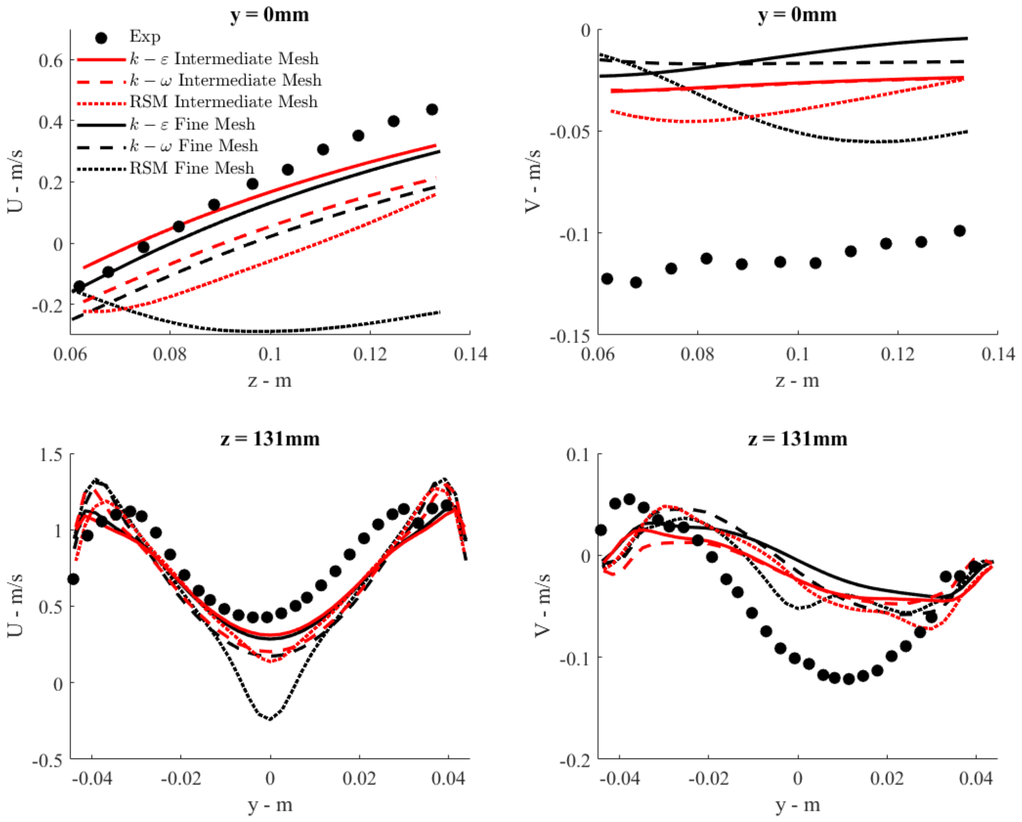

Figure 8 – axial and radial profiles of mean liquid axial velocity, U, and mean liquid y-velocity, V, at different axial and y coordinates as obtained from PIV measurements, Exp, and from the simulations with different turbulence models and different grids

The predictions of the intermediate grid show little deviations from those obtained with the fine grid, except for the profiles obtained with the RSM, that exhibits stronger grid dependency, as it can be observed by the large differences in the velocity profiles. The mean deviation between the numerical results and the experiments was calculated. The smallest mean deviations are found using the k-ε turbulence model, with deviations about 0.1 m/s. The mean deviation adopting the k-ω model is about twice that of the k-ε turbulence model, in the axial direction, while deviations larger than 0.4m/s are found with the RSM. The deviations on the radial component are less relevant, being the magnitude of the radial velocity smaller.

Together with the mean liquid velocity components, the liquid velocity fluctuations were also experimentally determined. A comparison between the experimental and numerical axial liquid root mean square velocity fluctuation, u, and radial liquid root mean square velocity fluctuation, v, is presented in Figure 9 and Figure 10 for the results obtained both with the intermediate and with the fine grid. For the RSM, the root mean square of the velocity fluctuations is obtained from the solution of the Reynolds stresses transport equation. For the k-ε and k-ω models, the root mean square velocity fluctuations were obtained from the turbulent kinetic energy as:

$$u = v = \sqrt{\frac{2}{3}k} \tag{17}$$

Figure 9 shows the axial profiles of u and v and, despite the adoption of a simplified turbulent descriptions, the agreement between experimental and numerical results is acceptable and consistent with what expected from RANS simulations. Also in this case, the RSM predicts profiles that differ the most from the experimental trends. In particular, the RSM predicts liquid velocity fluctuation with opposite trends with respect to the experimental measurements, especially at lower axial coordinates. Conversely, the two-equations k-ε and k-ω turbulence models generally better describe the liquid velocity fluctuation trends, with the former model predicting a better agreement with the experiments. The mean deviations between experimental and numerical fluctuating velocity components were calculated, as previously done for the mean velocity components. Comparable deviations are found adopting the fine grid and the intermediate grid. Values below 0.05 m/s are generally found with all the adopted models and grids.

The liquid velocity fluctuations profiles along the vertical coordinate, shown in Figure 10, qualitatively agree with the experimentally observed trends. As shown by the axial profiles, the fluctuation magnitudes are underpredicted, with a general better agreement for the fluctuations obtained with the k-ε turbulent model. The maximum deviations between experimental and numerical results are found towards the pipe walls. The mean deviations on both velocity fluctuations components are in the order of 0.1 m/s, with small variations depending on the turbulence model adopted.

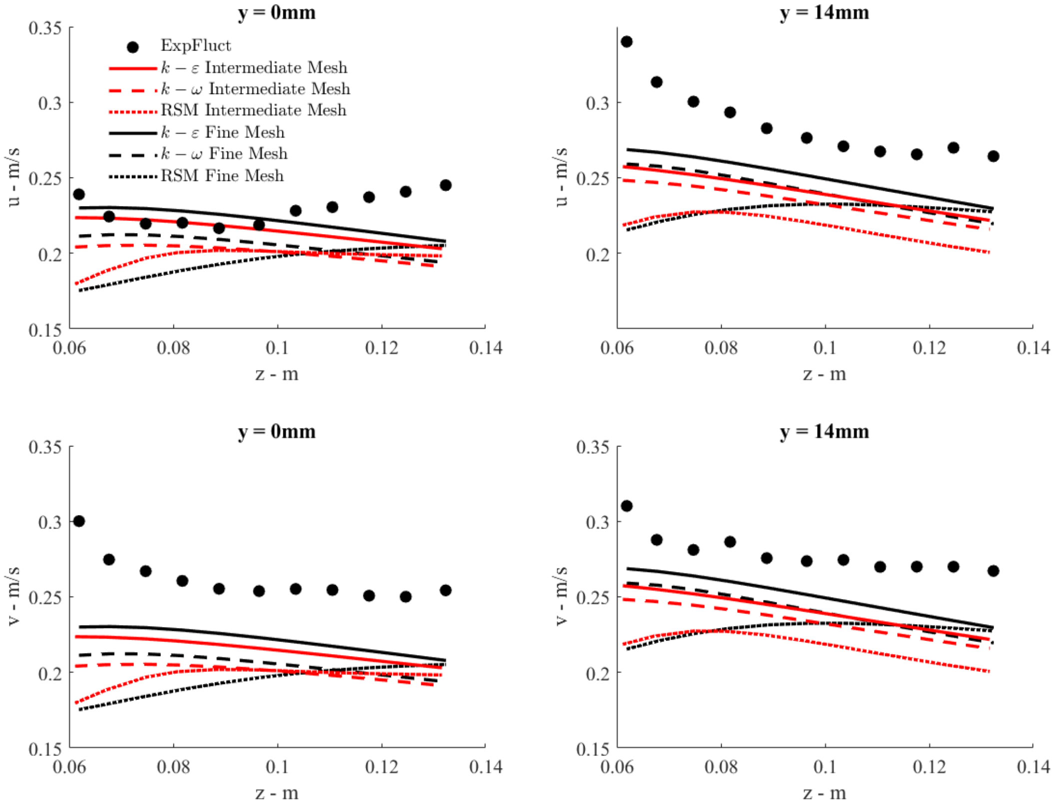

Figure 9 – axial profiles of the liquid axial velocity fluctuations, u, and the liquid y-velocity fluctuations, v, at different y-coordinates as obtained from PIV measurements, Exp, and from the simulations with different turbulence models and different grids

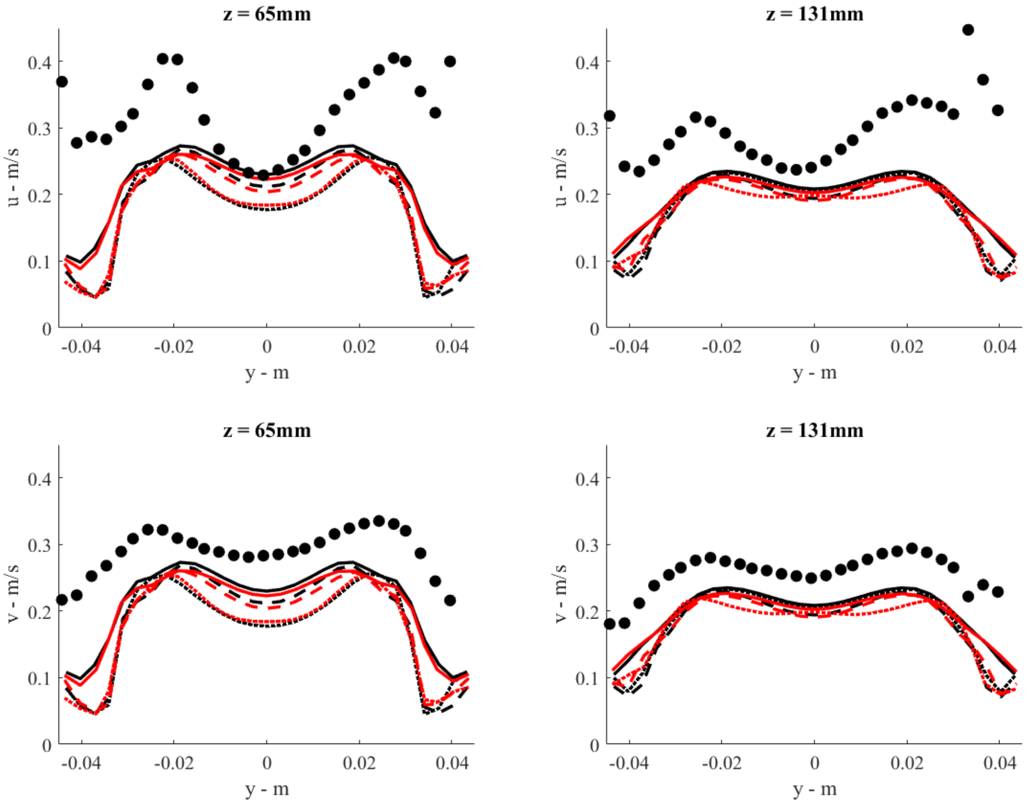

Figure 10 –profiles of the liquid axial velocity fluctuations, u, and the liquid y-velocity fluctuations, v, along the y-coordinate at different axial positions as obtained from PIV measurements, Exp, and from the simulations with different turbulence models and different grids. The legend is the same as in Figure 9

Figure 9 and Figure 10 confirm that the grid has a negligible effect on the prediction of the fluctuating velocities, and, as in the case of the mean velocity profiles shown in Figure 8, the largest differences are observable on the fluctuating velocity profiles obtained with the RSM turbulence model.

From the analysis of the single-phase flow field, it can be concluded that the k-ε turbulence model better describes the mean and fluctuating liquid flow fields in the system, despite the swirling flow generated by the static separator device. The reason may be that the tangential and radial velocity components are smaller than the axial velocity and therefore the limitation in the application of the k-ε turbulence model in this particular swirling flow are negligible. Moreover, as shown in Section 4, the RSM requires finer grids to reach grid independent results. This may contribute to the uncertainties observed in the comparison between the predictions of this model with experimental data.

Due to the differences in the computational times, the intermediate mesh was deemed to produce sufficiently reliable results and the two-phase simulations were conducted with such grid.

5.2 Gas-liquid simulations with a constant bubble size

Having quantified the effect of the grids on the results, gas-liquid simulations with the intermediate grid were performed, with a liquid flow rate of 25 m^3/h, a gas flow rate of 7.5 L/min (0.45 m^3/h) and a constant bubble diameter inferred from experimental observations. Results from the different turbulence models were compared against experimental observations in the same operative conditions.

The normalized average of the gas distribution, Figure 11, obtained as described in Section 2, shows that in gas-liquid operations the lighter phase collects towards the centre of the pipe due to the swirling flow. In these operative conditions, the apparent acceleration due to the centrifugal force is larger than the gravitational acceleration up to 3.15 pipe diameters downwind the swirler. This acceleration is larger than 50% of g up to 6.1 pipe diameters, and then it decreases as the flow moves downstream. Therefore, immediately after the swirler, gravity is overcome by the centrifugal acceleration, and up to 6 pipe diameters the magnitude of the relative forces is comparable. The high centrifugal acceleration determines the gas accumulation in the central zone of the pipe.

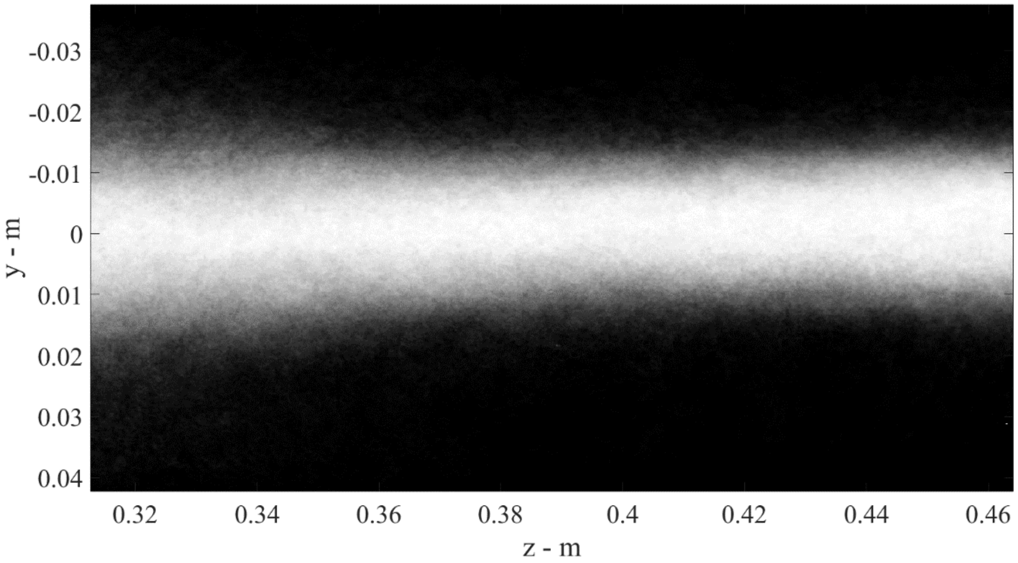

Figure 11 – normalized average of the gas-phase distribution on a vertical pipe section. The white hue is proportional to the gas phase hold-up while the black color represents the liquid phase. The flow develops from left to right.

The gas accumulating in the zone immediately downstream of the swirler is observed to produce a conic shape, while transitioning to a cylindrical shape as the flows moves at higher axial coordinates. Figure 11 clearly shows the central cylindrical zone in which the lighter gas-phase accumulates and at low axial coordinates the terminal part of the cone zone forming behind the inline swirler is visible.

Collecting several pictures of the system as described in Section 2, it was possible to calculate the bubble Probability Density Function (PDF) in the zone around the central core of gas accumulation and the results are shown in Figure 12.

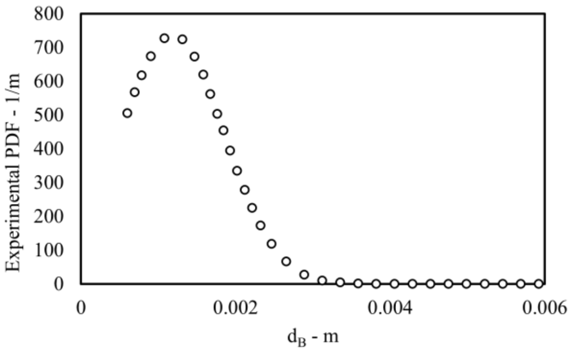

Figure 12 – bubble probability density function measured around the central core of gas accumulation

The PDF shown in Figure 12 is not representative of the whole bubble population, since towards the centre larger bubbles are expected, but due to the higher gas accumulation in this zone, determining optical inaccessibility, a bubble size could not be directly measured. Based on the PDF shown in Figure 12, a constant bubble diameter equal to 1.2 mm was used as a first guess bubble size to obtain a gas-liquid flow field from which derive preliminary information. In Figure 13 the gas volume fraction distribution on a vertical plane passing through the centre of the pipe is shown, together with the experimental gas hold up distribution previously reported in Figure 11.

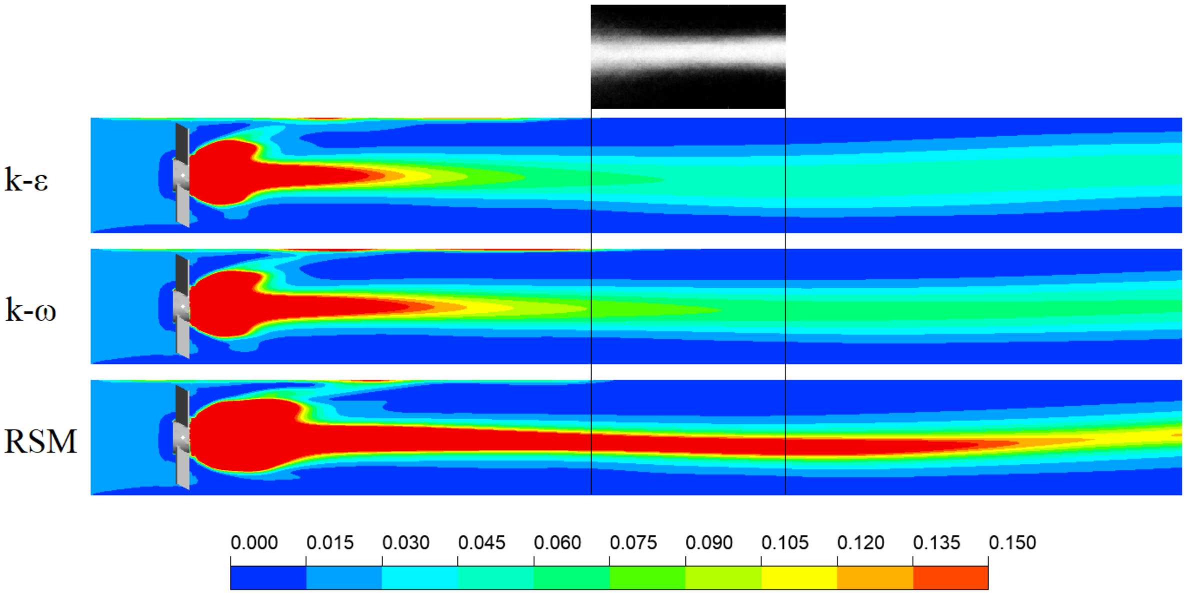

Figure 13 – gas volume fraction distribution on a vertical plane passing through the centre of the pipe, as obtained with different turbulence models. The flow develops from left to right. On the top, the experimental hold-up distribution, as shown in Figure 11, is reported for direct comparison.

Figure 13 shows that qualitatively similar gas volume fraction distributions are obtained adopting either the k-ε or the k-ω turbulence model. On the other hand, the RSM predicts a higher accumulation of gas towards the centre. The comparison with the experimental hold-up highlights that the numerical simulations overpredict the size of the central zone of accumulation. Since a single bubble diameter is considered, in the centre the bubble size is likely underestimated, allowing more gas to accumulate there. The difference in the average gas volume fraction profile as predicted by the different models is shown in Figure 14.

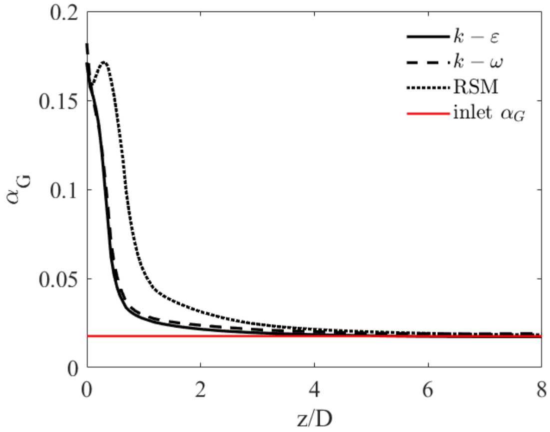

Figure 14 – axial profile of average gas volume fraction on the pipe sections, as obtained with different turbulence models, as a function of the non-dimensional axial coordinate z/D. The gas volume fraction entering the pipe, inlet α_G*, is also reported*

The section-average axial profiles of the gas volume fractions shown in Figure 13 are reported in Figure 14. The analysis of these two figures highlights that firstly gas accumulates in the region downstream of the swirler hub, then a cylindrical central region with high gas volume fraction develops, confining the gas phase towards the centre of the pipe. This behavior is also experimentally observed with the formation of the conical and the cylindrical central core of gas accumulation. The cone axial evolution, identified by the sharp reduction in average gas volume fraction observable in Figure 14, is analogously predicted by all the three turbulence models. The gas volume fraction axial gradient is very similar, but the zone predicted by the RSM is shifted towards higher axial coordinates. The zone affected by the swirler presence can be defined as the distance from the swirler at which the gas volume fraction recovers a value of ±5% of the inlet volume fraction value, and it is equal to 3.9 pipe diameters for the k-ε model, and 6.8 pipe diameters for both the RSM and the k-ω model. Close to the swirler a noticeable drift velocity between the two phases is induced, that causes a gas accumulation as show by the average gas volume fraction axial profile. At a distance larger than 3.9-6.8 pipe diameters, depending on the turbulent model used, the drift velocity is practically negligible and therefore the average gas volume fraction becomes equal to the ratio of the gas and the mixture flowrates. This information can be useful to design the equipment to remove the gas fraction from the liquid stream. The axial extension of the cone zone is underpredicted by all the simulations, since this zone disappears at a distance of 1.1-1.7 pipe diameters from the swirler, while it was experimentally observed to last up to 3.3 pipe diameters.

Based on the results of this Section and Section 5.1, the k-ε turbulence model was deemed to be the most suitable to describe the fluid flow generating in the pipe equipped with the swirling inline separator, since it better describes the single-phase and produces realistic gas-liquid distributions. For these reasons, the k-ε turbulence model was adopted in the simulations where the bubble size was determined from a population balance approach.

5.3 Gas-liquid simulations with bubble size determined with a population balance approach

Starting from the gas-liquid flow field obtained with a constant bubble diameter and the k-ε turbulence model, the population balance equation presented in Section 3.2) is solved either in a frozen flow field, thus decoupling the solution of the flow equations from the PBE, or simultaneously with the flow equations, thus obtaining a coupled solution. The simulations are performed with the intermediate grid, with a liquid flow rate of 25 m^3/h and a gas flow rate of 7.5 L/min (0.45 m^3/h).

The Sauter mean diameter distributions predicted by the two approaches are reported in Figure 15.

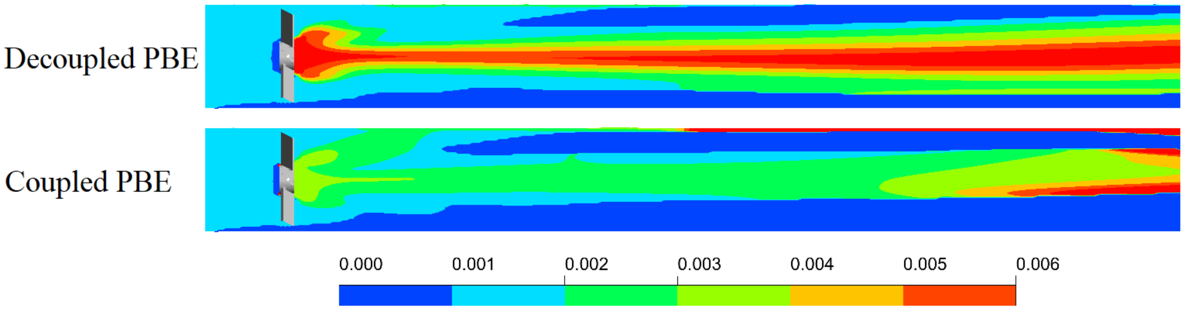

Figure 15 – Sauter mean diameter distribution on a vertical plane as obtained either with a decoupled or a coupled solution of the PBE with the flow equations. Color scale in m

Figure 15 shows that the bubble Sauter mean diameters predicted with a decoupled approach are larger than those predicted with a coupled approach. Since the flow field is frozen and the interphase forces acting on the dispersed phase do not change with the size of the bubbles, very large bubbles accumulate in the central slower zone. Conversely, in the coupled solution the interphase forces change depending on the local bubble size and just bubbles smaller than a critical size are collected in the centre. Larger bubbles move away from the slower central zone towards the top of the pipe where higher turbulent dissipation rates enhance breakup. As a result, the bubble Sauter mean diameter distribution is much narrower when the PBE is solved together with the flow equations, Figure 16.

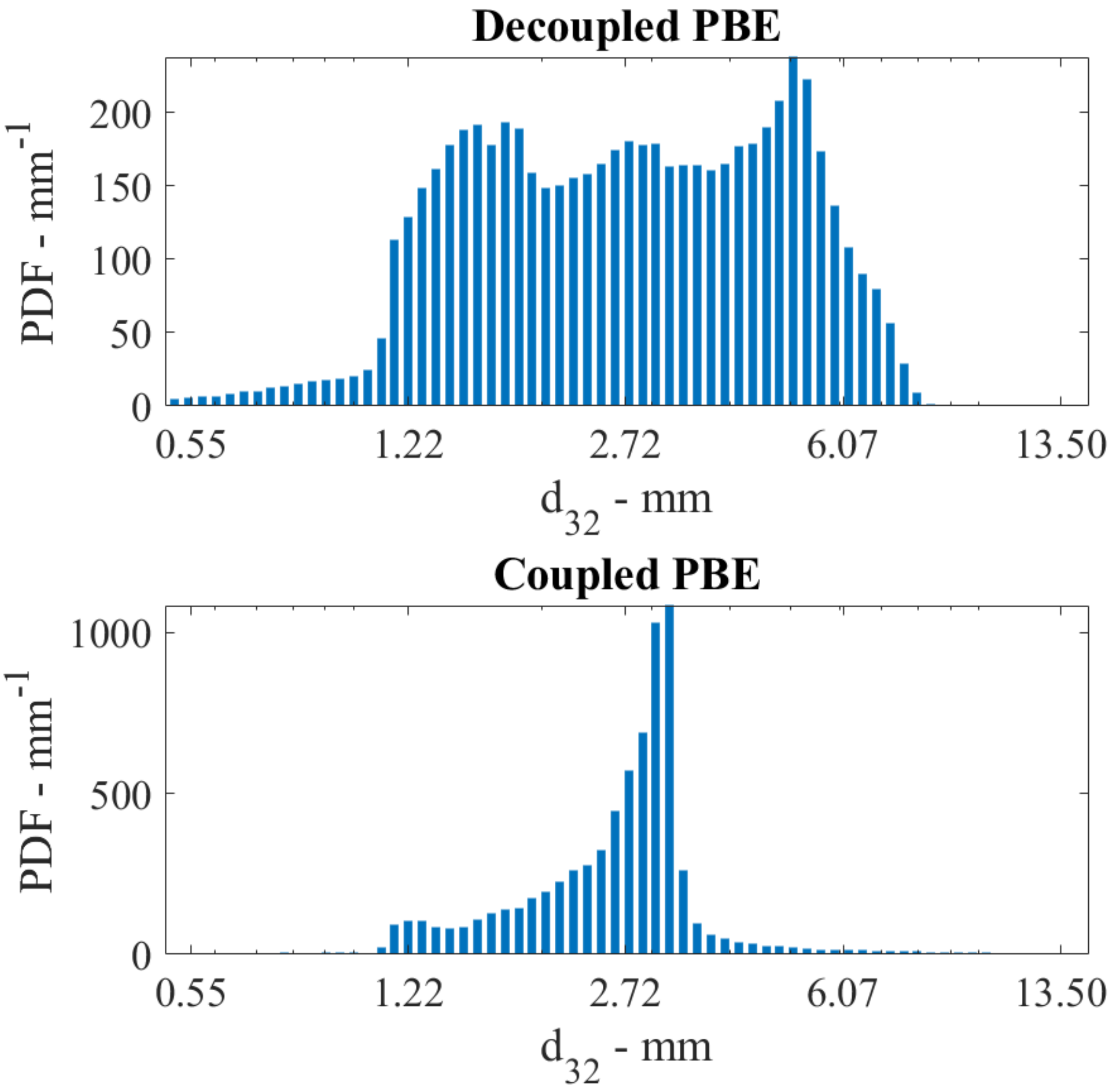

Figure 16 – mass weighted Sauter mean bubble diameter distribution in the system, as obtained either with a decoupled or a coupled solution of the PBE with the flow equations.

The PDF reported in Figure 16 is obtained by weighting the d_{32} on the gas mass and it is evident how the coupled solution of PBE and flow equations leads to a narrower Sauter mean diameter distribution. Interestingly, the bubble distribution is asymmetrical and very few bubbles larger than 3-3.5 mm are present in the pipe, due to the breakup of the larger bubbles that rise towards the high-turbulent-dissipation top section of the pipe.

The bubble size distribution (BSD) obtained by the coupled solution of the PBE and the flow equations was compared with the experimentally determined BSD, and the results are presented as probability density functions in Figure 17. The numerical bubble size number distribution function was reconstructed assuming a lognormal distribution, where its mean and variance were obtained from the transported moments with an iterative procedure [35]. The NDF moments were volume averaged on the pipe section experimentally investigated for the determination of the NDF around the central core of gas accumulation. The investigated zone has an axial extension from 0.45m to 0.56m and a radial extension from 0.02m to 0.04m. The volume averaged moments were adopted in the moment-inversion algorithm, to obtain the PDF shown in Figure 17.

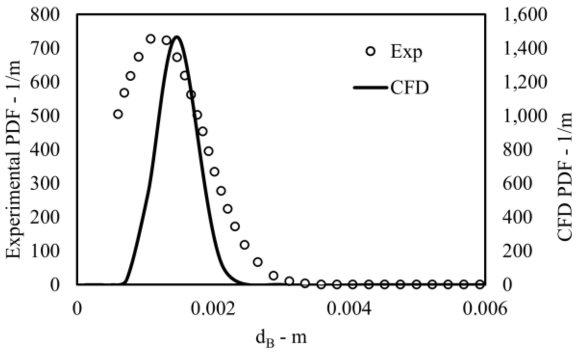

Figure 17 – Experimental (Exp) and numerical (CFD) probability density function around the central core of gas accumulation

Figure 17 shows that a reasonable agreement was obtained between the experimental and numerical results. In both cases, a relatively narrow distribution was observable, with a numerical mean value, d_{10}, of 1.4 mm and 1.3 mm for the experimental and numerical BSD, respectively. As discussed in Section 4), a discrepancy between the work done by the pressure drop and the total turbulent energy dissipation exists, probably due to an underprediction of the turbulent variables due to an insufficient grid density [36,40]. This translates to a possible dependency of the calculated bubble size from the domain discretization, which is inevitable for most of practical applications. With the intermediate grid and the k-ε model adopted to obtain the results presented in this section, the underprediction of the turbulent dissipation rate is around 29%. Grid independent kernel parameter values together with a grid dependent scalar correction in the formulation of the kernels, previously proposed and tested [40,42], may contribute to improve the agreement between numerical and experimental BSD. Moreover, a better agreement may be reached considering different kernels to model breakup and coalescence phenomena. The adopted kernels, albeit being computationally cheap, introduce uncertainties in the calculation of the daughter distribution function [42] and in the effect of the turbulent dissipation rate [33,43]. More advanced breakup and coalescence kernels will be tested in future works. Despite the discussed limitations of the computational approach, the presented method produces a realistic bubble size distribution that reasonably agrees with the experimental data.

The gas volume fraction distribution obtained from the coupled solution of the PBE is reported in Figure 18 and it is qualitatively similar to the gas volume fraction distribution obtained with a constant bubble diameter, observed in Figure 13.

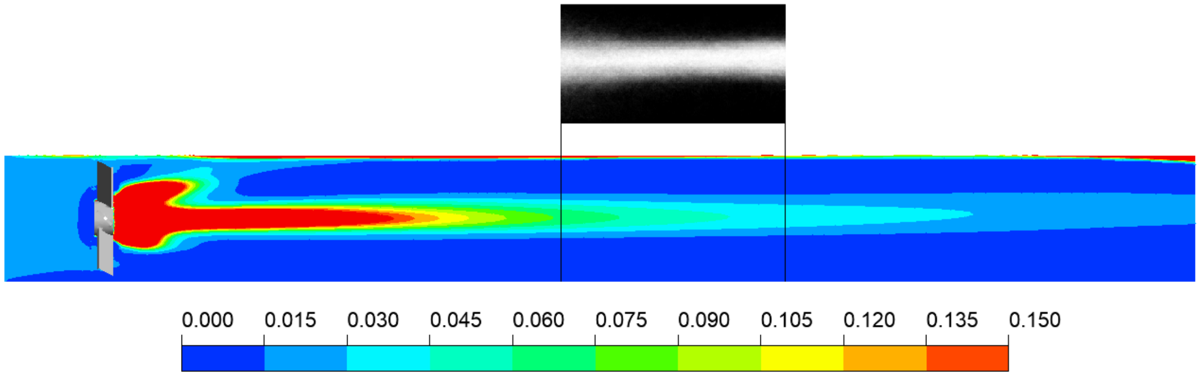

Figure 18 gas volume fraction distribution on a vertical plane passing through the centre of the pipe, as obtained from the coupled solution of the PBE. The flow develops from left to right. On the top, the experimental hold-up distribution, as shown in Figure 11, is reported for direct comparison.

Figure 18 shows that larger bubbles that result from coalescence phenomena reach the top of the pipe, where they flow touching the upper inner wall of the pipe, since the increased buoyancy does not allow for these bubbles to be re-entrained in the bulk of the flow. This results in a smaller central zone of gas accumulation that is in better agreement with the experimental hold-up distribution, compared to the single bubble diameter approach shown in Figure 13.

To obtain practical information on the gas distribution, the size of the central cylindrical zone in which the gas accumulates is calculated for both the coupled PBE simulation and the experimental set-up. It should be pointed out that a direct comparison between numerical gas volume fraction and hold-up determined from the experiments is not possible, since it is not possible to correlate the gray scale to a gas volume fraction value. Nonetheless the size of the central gas accumulation zone was calculated as the limit on which a value of white equal to 0.1 was found, averaged on a 1cm moving window, roughly corresponding to the discernable black-white interface observable in Figure 11. This experimental profile was compared with the size of the central cylindrical zone obtained from the numerical simulation with a coupled PBE solution and the results are compared in Figure 19.

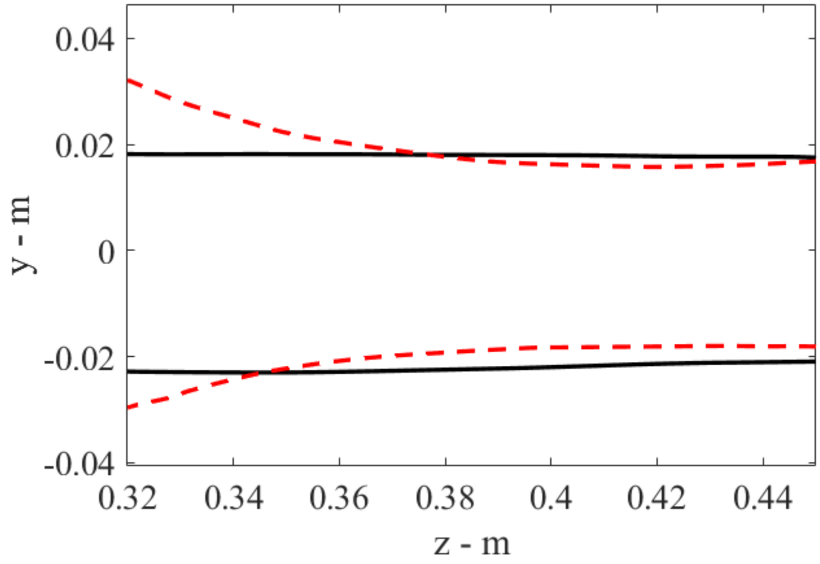

Figure 19 – profiles of the central zone of gas accumulation as experimentally determined, dashed red lines, and as predicted from the coupled PBE simulation, black solid lines. The experimental gas accumulation extension was identified with a white hue threshold of 0.1, while the numerical gas accumulation extension was identified with a gas volume fraction threshold of 0.01.

Figure 19 shows that the numerical simulation predicts the size of the central cylindrical zone of gas accumulation in sufficient agreement with the experimentally determined one. These results prove that the proposed computational approach can be adopted for simulating the gas-liquid flow field generated by a swirling inline separator. The numerical simulations may help in troubleshooting and design this kind of separators, while also aiding in the design and positioning of the equipment needed to extract the segregated gas-liquid phases.

6. Conclusions

A numerical approach for the simulation of inline swirler for gas-liquid operations is validated with single-phase and gas-liquid experimental data. The comparison allowed to test different turbulence models and the k-ε turbulence model provided better predictions in single-phase applications, with realistic predictions of the gas-liquid flow field.

A population balance model coupled with the flow equations revealed that the Sauter mean bubble diameter distribution is relatively narrow, since the breakup phenomena occurring towards the periphery of the pipe reduce the size of the larger bubbles migrating towards the top of the pipe. As expected, this phenomenon is not captured by decoupling the solution of the PBE from the flow equations.

The proposed and validated computational approach allows to satisfactorily predict the bubble size distribution and the size of the central cylindrical core of gas accumulation. It also provides useful information on the gas accumulation zone, which may be exploited to design and position devices for the gas removal from the pipe.

Future work will be addressed to improve the predictions of the gas-liquid distribution, especially close to the swirler with more comprehensive turbulent models, turbulent interactions, and interphase forces. The adoption of more advanced breakup and coalescence kernels, the effect of grid independent kernel parameters and a scalar correction in the PBE kernels will be tested to quantify the effect of the turbulent dissipation rate on the BSD.

7. References

[1] D.W. Green, R.H. Perry, Perry's chemical engineers' handbook, 8th Editio, McGraw-Hill, 2008.

[2] R.B. Bird, W.E. Stewart, E.N. Lightfoot, Transport Phenomena, Wiley & Sons, Inc., New York, 1960.

[3] S. Szepessy, P. Thorwid, Low Energy Consumption of High-Speed Centrifuges, Chem. Eng. Technol. 41 (2018) 2375–2384. https://doi.org/10.1002/ceat.201800292.

[4] A.I. Stankiewicz, J.A. Moulijn, Process intensification: Transforming chemical engineering, Chem. Eng. Prog. 96 (2000) 22–33.

[5] W.W.F. Leung, Centrifugal Separations in Biotechnology, Elsevier, 2007.

https://doi.org/10.1016/B978-1-85617-477-0.X5000-9.

[6] Z. Zhang, R. Liao, Z. Cai, J. Liu, An orthogonal numerical simulation experiment study towards the decay characteristics and effective swirl length of the swirling flow in a vortex tool inserted tube, J. Nat. Gas Sci. Eng. 76 (2020) 103220. https://doi.org/10.1016/j.jngse.2020.103220.

[7] J. Yin, Y. Ma, Y. Qian, D. Wang, Experimental investigation of the bubble separation route for an axial gas–liquid separator for TMSR, Ann. Nucl. Energy. 97 (2016) 1–6. https://doi.org/10.1016/j.anucene.2016.06.018.

[8] K.A. Maurice Stewart, Gas-Liquid And Liquid-Liquid Separators, Elsevier, 2008. https://doi.org/10.1016/B978-0-7506-8979-3.X0001-3.

[9] R.A. Putra, T. Schäfer, M. Neumann, D. Lucas, CFD studies on the gas-liquid flow in the swirl generating device, Nucl. Eng. Des. 332 (2018) 213–225. https://doi.org/10.1016/j.nucengdes.2018.03.034.

[10] F. Zidouni, E. Krepper, R. Rzehak, S. Rabha, M. Schubert, U. Hampel, Simulation of gas–liquid flow in a helical static mixer, Chem. Eng. Sci. 137 (2015) 476–486. https://doi.org/10.1016/j.ces.2015.06.052.

[11] B. Cai, J. Wang, L. Sun, N. Zhang, C. Yan, Experimental study and numerical optimization on a vane-type separator for bubble separation in TMSR, Prog. Nucl. Energy. 74 (2014) 1–13. https://doi.org/10.1016/j.pnucene.2014.02.007.

[12] R. Rzehak, E. Krepper, Bubbly flows with fixed polydispersity: Validation of a baseline closure model, Nucl. Eng. Des. 287 (2015) 108–118. https://doi.org/10.1016/j.nucengdes.2015.03.005.

[13] R.A. Putra, M. Neumann-Kipping, T. Schäfer, D. Lucas, Comparison of Gas–Liquid Flow Characteristics in Geometrically Different Swirl Generating Devices, Energies. 12 (2019) 4653. https://doi.org/10.3390/en12244653.

[14] F. Yuan, Z. Cui, J. Lin, Experimental and Numerical Study on Flow Resistance and Bubble Transport in a Helical Static Mixer, Energies. 13 (2020) 1228. https://doi.org/10.3390/en13051228.

[15] A. Paglianti, G. Montante, Simultaneous measurements of liquid velocity and tracer concentration in a continuous flow stirred tank, Chem. Eng. Sci. 216 (2020) 115495. https://doi.org/10.1016/j.ces.2020.115495.

[16] G. Montante, D. Horn, A. Paglianti, Gas–liquid flow and bubble size distribution in stirred tanks, Chem. Eng. Sci. 63 (2008) 2107–2118. https://doi.org/10.1016/j.ces.2008.01.005.

[17] D.C. Wilcox, Turbulence Modeling for CFD (Third Edition), 3rd ed., Birmingham Press, Inc, San Diego, California, 2006. http://www.dcwindustries.com (accessed June 7, 2022).

[18] H.. Versteeg, W. Malalasekera, An Introduction to Computational Fluid Dynamics - The Finite Volume Method, 2nd ed., Pearson Education Limited, Harlow, England (UK), 2007.

[19] J.O. HINZE, TURBULENCE, McGraw-Hill Publishing Co., New York, 1975. https://books.google.com/books/about/Turbulence.html?id=DfRQAAAAMAAJ (accessed June 7, 2022).

[20] K. Ekambara, R.S. Sanders, K. Nandakumar, J.H. Masliyah, CFD simulation of bubbly two-phase flow in horizontal pipes, Chem. Eng. J. 144 (2008) 277–288. https://doi.org/10.1016/j.cej.2008.06.008.

[21] M. Simonnet, C. Gentric, E. Olmos, N. Midoux, Experimental determination of the drag coefficient in a swarm of bubbles, Chem. Eng. Sci. 62 (2007) 858–866. https://doi.org/10.1016/j.ces.2006.10.012.

[22] F. Maluta, A. Paglianti, G. Montante, Prediction of gas cavities size and structure and their effect on the power consumption in a gas-liquid stirred tank by means of a two-fluid RANS model, Chem. Eng. Sci. 241 (2021) 116677. https://doi.org/10.1016/j.ces.2021.116677.

[23] F. Maluta, A. Paglianti, G. Montante, Two-fluids RANS predictions of gas cavities, power consumption, mixing time and oxygen transfer rate in an aerated fermenter scale-down stirred with multiple impellers, Biochem. Eng. J. 166 (2021) 107867. https://doi.org/10.1016/j.bej.2020.107867.

[24] M. Ishii, N. Zuber, Drag coefficient and relative velocity in bubbly, droplet or particulate flows, AIChE J. 25 (1979) 843–855. https://doi.org/10.1002/aic.690250513.

[25] L. Schiller, A. Naumann, Über die grundlegenden berechnungen bei der schwerkraftbereitung, Zeitschrift Des Vereines Dtsch. Fngenieure. 77 (1933) 318--321.

[26] A.D. Burns, T. Frank, I. Hamill, J.-M.M. Shi, The Favre Averaged Drag Model for Turbulent Dispersion in Eulerian Multi-Phase Flows, in: Fifth Int. Conf. Multiph. Flow, ICMF-2004, Yokohama, Japan, 2004: pp. 1–17.

[27] H. Luo, H.F. Svendsen, Theoretical model for drop and bubble breakup in turbulent dispersions, AIChE J. 42 (1996) 1225–1233. https://doi.org/10.1002/aic.690420505.

[28] J. Solsvik, S. Tangen, H.A. Jakobsen, On the constitutive equations for fluid particle breakage, Rev. Chem. Eng. 29 (2013) 241–356. https://doi.org/10.1515/revce-2013-0009.

[29] A. Buffo, D.L. Marchisio, Modeling and simulation of turbulent polydisperse gas-liquid systems via the generalized population balance equation, Rev. Chem. Eng. 30 (2014) 73–126. https://doi.org/10.1515/revce-2013-0015.

[30] M.J. Prince, H.W. Blanch, Bubble coalescence and break-up in air-sparged bubble columns, AIChE J. 36 (1990) 1485–1499. https://doi.org/10.1002/aic.690361004.

[31] C.A. Coulaloglou, L.L. Tavlarides, Description of interaction processes in agitated liquid-liquid dispersions, Chem. Eng. Sci. 32 (1977) 1289–1297. https://doi.org/10.1016/0009-2509(77)85023-9.

[32] L. Niño, R. Gelves, H. Ali, J. Solsvik, H. Jakobsen, Applicability of a modified breakage and

coalescence model based on the complete turbulence spectrum concept for CFD simulation of gas-liquid mass transfer in a stirred tank reactor, Chem. Eng. Sci. 211 (2020) 115272. https://doi.org/10.1016/j.ces.2019.115272.

[33] S. Castellano, L. Carrillo, N. Sheibat-Othman, D. Marchisio, A. Buffo, S. Charton, Using the full turbulence spectrum for describing droplet coalescence and breakage in industrial liquid-liquid systems: Experiments and modeling, Chem. Eng. J. 374 (2019) 1420–1432. https://doi.org/10.1016/j.cej.2019.06.032.

[34] J. Baldyga, W. Podgórska, Drop break-up in intermittent turbulence: Maximum stable and transient sizes of drops, Can. J. Chem. Eng. 76 (1998) 456–470. https://doi.org/10.1002/cjce.5450760316.

[35] D.L. Marchisio, R.O. Fox, Computational Models for Polydisperse Particulate and Multiphase Systems, Cambridge University Press, Cambridge, 2013. https://doi.org/10.1017/CBO9781139016599.

[36] M. Coroneo, G. Montante, A. Paglianti, F. Magelli, CFD prediction of fluid flow and mixing in stirred tanks: Numerical issues about the RANS simulations, Comput. Chem. Eng. 35 (2011) 1959–1968. https://doi.org/10.1016/j.compchemeng.2010.12.007.

[37] P.J. Roache, Verification and Validation in Computational Science and Engineering, Hermosa Publishers, Albuquerque, New Mexico, 1998. http://www.hermosa-pub.com/hermosa (accessed April 20, 2017).

[38] A. Vikhansky, CFD modelling of turbulent liquid–liquid dispersion in a static mixer, Chem. Eng. Process. - Process Intensif. 149 (2020) 107840. https://doi.org/10.1016/j.cep.2020.107840.

[39] F. Azizi, W. Abou-Hweij, N. Lebaz, N. Sheibat-Othman, A numerical evaluation of flows through an SMX-Plus mixer, Chem. Eng. Res. Des. 178 (2022) 382–394. https://doi.org/10.1016/j.cherd.2021.12.030.

[40] F. Maluta, A. Buffo, D. Marchisio, G. Montante, A. Paglianti, M. Vanni, Effect of turbulent kinetic

energy dissipation rate on the prediction of droplet size distribution in stirred tanks, Int. J. Multiph. Flow. 136 (2021) 103547. https://doi.org/10.1016/j.ijmultiphaseflow.2020.103547.

[41] Z. Gao, D. Li, A. Buffo, W. Podgórska, D.L. Marchisio, Simulation of droplet breakage in turbulent liquid–liquid dispersions with CFD-PBM: Comparison of breakage kernels, Chem. Eng. Sci. 142 (2016) 277–288. https://doi.org/10.1016/j.ces.2015.11.040.

[42] F. Maluta, A. Buffo, D. Marchisio, G. Montante, A. Paglianti, M. Vanni, Numerical and Experimental Analysis of the Daughter Distribution in Liquid-Liquid Stirred Tanks, Chem. Eng. Technol. 44 (2021) 1994–2001. https://doi.org/10.1002/ceat.202100237.

[43] Y. Liao, D. Lucas, A literature review of theoretical models for drop and bubble breakup in turbulent dispersions, Chem. Eng. Sci. 64 (2009) 3389–3406. https://doi.org/10.1016/j.ces.2009.04.026.